Received: 00 Month 0000 | Revised: 00 Month 0000 | Accepted: 00 Month 0000

DOI: xxx/xxxx

ARTICLE TYPE

A comparative CFD study of four inferior vena cava filters

Josep M. López*[1] | Gerard Fortuny[1] | Dolors Puigjaner[1] | Joan Herrero[2] | Francesc Marimon[3]

[1]Departament d' Enginyeria Informàtica i Matemàtiques, Universitat Rovira i Virgili. Tarragona, Catalunya, Spain
[2]Departament d' Enginyeria Química, Universitat Rovira i Virgili. Tarragona, Catalunya, Spain
[3]Departament de Medicina i Cirurgia, Universitat Rovira i Virgili. Tarragona, Catalunya, Spain

Correspondence
*Josep M. López, Departament d' Enginyeria Informàtica i Matemàtiques, Universitat Rovira i Virgili, Av Països Catalans 26, Tarragona, Catalunya, Spain.
Email: josep.m.lopez@urv.cat

Summary

Computational fluid dynamics was used to simulate the flow of blood within an inferior vena cava (IVC) geometry model that was reconstructed from computed tomography images obtained from a real patient. The main novelty of the present work is that we simulated the implantation of four different filter models in this realistic IVC geometry. We considered different blood flow rates in the range between $V_{in} = 20$ and $V_{in} = 80\ cm^3/s$ and all simulations were performed with both the Newtonian and a non–Newtonian model for the blood viscosity. We compared the hemodynamics performance of the different filter models and we paid a special attention to the total drag force, F_d, exerted by the blood flow on the filter surface. This force is the sum of two contributions: the viscous skin friction force, which was found to be roughly proportional to the filter surface area, and the pressure force, which depended on the particular filter geometry design. The F_d force is relevant because it must be balanced by the total force exerted by the filter hooks/struts on the IVC wall at the attachment locations. For the highest V_{in} value investigated, the variation in F_d among filters was from 116 to 308 dyne. We also showed how the present results can be extrapolated to obtain good estimates of the drag forces if the blood viscosity levels change, i.e., if the patient with a filter implanted is treated with anticoagulant therapy.

KEYWORDS:
Inferior vena cava filters, Computational fluid dynamics, Wall shear stress, Hemodynamics, Non–Newtonian viscosity model, Drag coefficients

1 | INTRODUCTION

Pulmonary embolism (PE) is a life–threatening disease that occurs when a blood clot or parts of it become lodged in the pulmonary vascular system and obstruct blood flow. Most often PE is a consequence of deep venous thrombosis (DVT), which is in turn a major complication of cancer or orthopedic surgery, among others. Venous thromboembolism (DVT and/or PE) has an incidence of 1.4 to 2.2 per 1000 persons–year among US citizens aged over 45, and mortality rate is approximately 25% in the first 30 days.[1,2] In order to prevent PE, DVT patients are usually treated with anticoagulant drugs.[3] However, in patients who have contraindications or are unresponsive to anticoagulation therapy the placement of a filter into the inferior vena cava (IVC) is indicated.[2,4] These filters are devices specifically designed to capture blood clots that are transported by the blood flow within the vein. They are made of titanium or metal alloys and they are available in a good variety of models. At first, IVC filters were designed to be permanent but recently manufacturers have devised retrievable filter designs. Retrievable filters are preferable when the contraindications to anticoagulant drugs are considered temporary.[5]

There is some controversy in the medical community on the efficacy and safety of IVC filter placement. A relevant reference is the clinical study of Decousus et al.[6] These authors concluded that the implantation of an IVC filter brought no statistically significant benefit to patients following anticoagulant therapy. Moreover, the short term benefit of filter implantation in terms of reduced PE occurrence might be counterbalanced by complications such as IVC thrombosis, tilting, migration or fracture of the filter, recurrent DVT and penetration of the filter prongs into the IVC wall.[7–9] On the other hand, a recent clinical study on a large basis of 1200 individuals suggested the convenience of IVC filter placement in those DVT patients with diagnosed PE even if such patients were also receiving anticoagulant therapy.[10]

Several researchers investigated, either experimentally or computationally, how the presence of IVC filters affects the flow in simplified straight tube geometries.[11–15] These studies aimed to detect low pressure regions in the flow and areas with high wall shear stress (WSS) levels either in the tube wall or in the filter surfaces. The recent studies of Aycock et al[16,17] with one particular IVC filter model have brought to light that the use of an IVC geometry model based on a real patient predicts more extremal values of pressure–drop and WSS than the ones predicted by simplified or patient–averaged IVC models. One further conclusion of Aycock et al,[17] in regard of hemorheology, is that the use of non-Newtonian models of viscosity ought to be preferred in future studies in IVC hemodynamics.

In the present study computational fluid dynamics (CFD) is used to simulate the flow of blood within an IVC geometry model that was reconstructed from computed tomography (CT) images obtained from a real patient. The main novelty of the present work is that we simulate the implantation of four different filter models in this realistic IVC geometry. The hemodynamics performance of the different filter models is compared and a special attention is given to the total drag force, F_d, exerted by the blood flow on the filter surface. The total drag force is a very relevant quantity as F_d must be balanced by the total force exerted by the filter hooks/struts on the IVC wall at the attachment locations. We discuss and quantify the dependence of F_d, as well as other relevant quantities, on the particular value of the blood flow rate. Following Cheng et al,[18] infrarenal and supraceliac IVC blood flow rates of respectively $20\,\mathrm{cm}^3/\mathrm{s}$ ($1.2\,\mathrm{L/min}$) and $34\,\mathrm{cm}^3/\mathrm{s}$ ($2.04\,\mathrm{L/min}$) were assumed for rest conditions. Since a patient with an implanted IVC filter may be enrolled in some physical activity we consider also higher blood flow rates up to $80\,\mathrm{cm}^3/\mathrm{s}$ ($4.8\,\mathrm{L/min}$) and $100\,\mathrm{cm}^3/\mathrm{s}$ ($6\,\mathrm{L/min}$) for the infrarenal and supraceliac regions, respectively; these values are in the low range of the measurements reported by Cheng et al[18] for exercise conditions (110 heartbeats/min on the average). We also show how the present results can be extrapolated to obtain good estimates of the drag forces if the blood viscosity levels change, i.e., if the patient with a filter implanted is treated with anticoagulant therapy.

2 | MODELS AND METHODS

2.1 | Geometry models

The model for an IVC segment was reconstructed from in vivo CT images of a 65 years old, male patient. The length of the segment along the vertical (z) axis was 14.1 cm. The geometry model includes part of the IVC infrarenal region and the entrance region of the two renal veins, as shown in Figure 1. A base surface mesh for the IVC segment, consisting of $n_v = 68,432$ triangles, was obtained from segmentation of the CT images using the 3DSlicer software.[19] The lumen areas at the IVC model inlet and outlet sections respectively were $A_{in} = 3.7\ \mathrm{cm}^2$ and $A_{out} = 5.1\ \mathrm{cm}^2$ and the area of the vein segment wall was $A_{wall} = 125.3\ \mathrm{cm}^2$.

The geometry models created for each of the four filters are shown in Figure 1 and their main features are summarized in Table 1. These geometry models were constructed, using the Blender software,[20] from data obtained from several sources: we generated a preliminary version of the four IVC filter models using pictures from manufacturers[21–24] as well as from the literature.[11,25,26] In these pictures, the filters are portrayed unfolded into an arbitrary shape. It is important to note that in the real placement process the IVC filter is inserted into the vein using a capsule that contains the folded filter. At the suitable moment, as deemed by the practitioner, the filter is unfolded to contact the IVC wall. Thus, we modified the angles in our preliminary models, while preserving the original lengths of their elements, to make their shape consistent with the diameter of our IVC geometry model (around 20 mm). These values of the angles were found to be in qualitative agreement with the corresponding estimates obtained from previously published radiographies.[11,27–30] Each of the four filter geometry models were then uploaded into the Salome-Meca suite[31] where the respective surface meshes were built. The total number of triangles in the filter surface meshes ranged between $n_f = 55,032$ and $130,468$, depending on the complexity of the filter shape. The four filter surface meshes were placed within the IVC surface mesh with the same inclination and with their tips slightly below the right renal vein.[32] Note that whereas the filter models possess either hexagonal or octagonal symmetry (see Figure 1), the vein lumen lacks

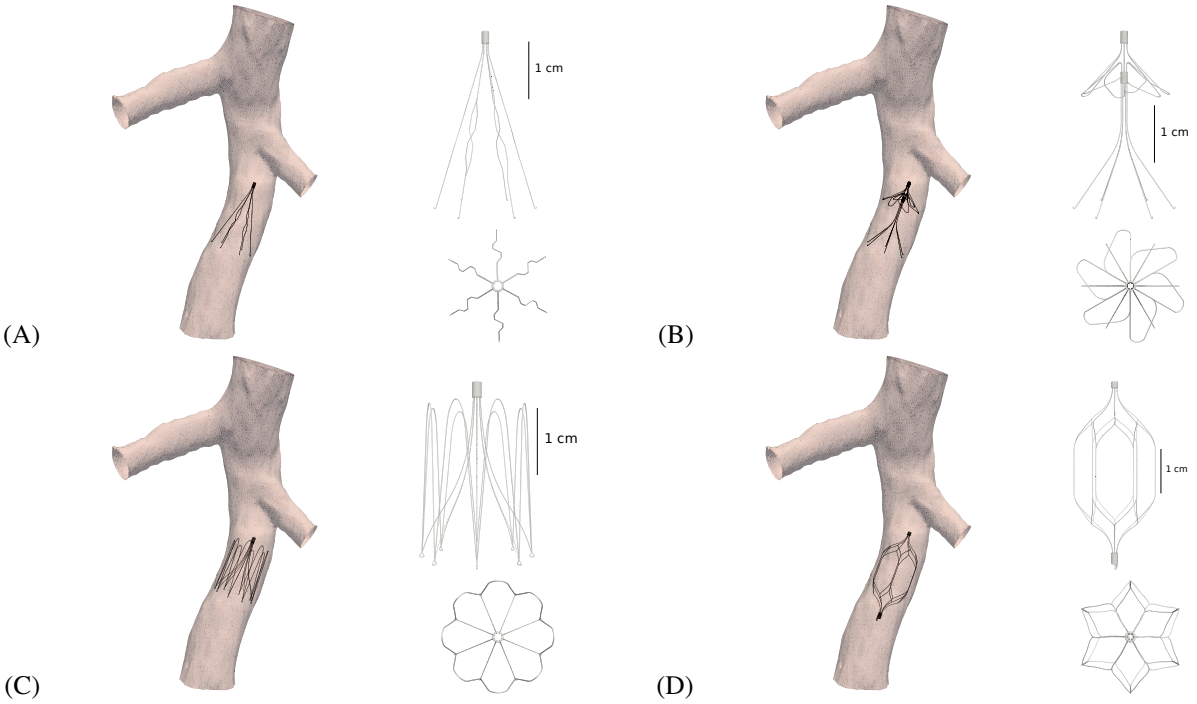

FIGURE 1 Posterior view of the IVC surface models with the filter placed inside, together with side and zenithal views of the four filter models: (A) filter 1; (B) filter 2; (C) filter 3; (D) filter 4. See the caption of Table 1 for the meaning of the filter labels 1 to 4.

	Filter			
Label	1	2	3	4
Commercial brand	Greenfield™, 21	SIMON NITINOL®, 22	VenaTech® Convertible™, 23	OPTEASE®, 24
Symmetry	Hexagonal	Hexagonal	Octogonal	Hexagonal
Type	Permanent	Permanent	Convertible	Optional
Surface area (m^2)	1.028×10^{-4}	1.882×10^{-4}	2.703×10^{-4}	1.965×10^{-4}

TABLE 1 Main features of the four filters investigated, which are labeled 1 to 4 for further references. Filter 3 is designated by the manufacturer as convertible because it can be operated to become folded against the IVC wall and thus unobtrusive to blood flow. Filter 4 is designated as optional because, according to the manufacturer, it may be either retrieved within a certain time window or be left in place with no significant additional risk for the patient health. The surface area of each filter model was calculated by numerical integration over the whole filter surface.

symmetry. To keep the filter axes well aligned with the blood main flow direction a small clearance between the filter hooks or struts and the vein wall, in the $0.2 - 1.0$ mm range, was allowed.

2.2 | Model and equations

The CFD simulations were performed using the OpenFOAM code[33]. The code solves numerically the differential mass and momentum conservation equations for an incompressible flow,

$$\frac{\partial U}{\partial t} + (U \cdot \boldsymbol{\nabla}) U = -\frac{1}{\rho}\boldsymbol{\nabla} p + \left\{ \boldsymbol{\nabla} \cdot \left[\left(\frac{\mu}{\rho} \right) \boldsymbol{\nabla} \right] \right\} U \tag{1}$$

$$\boldsymbol{\nabla} \cdot U = 0 \tag{2}$$

where $U = (u_x, u_y, u_z)$ is the velocity vector, ρ and μ are the fluid density and viscosity, respectively, and p is the pressure. Equations (1) and (2) were solved together with the usual no–slip boundary conditions at all solid walls and a convective boundary condition at the IVC outlet section. At the IVC and renal veins inlet sections the velocity distributions and pressure gradients were calculated under the fully developed flow assumption; see Fortuny et al.[34] for details.

A value of $\rho = 1060\,\mathrm{kg/m^3}$ was used for the blood density. Both the Newtonian fluid model, with $\mu = \mu_N = 3.45 \times 10^{-3}$ Pa·s, and the non–Newtonian Bird–Carreau viscosity model[35],

$$\mu = \mu(\gamma) = \mu_\infty + (\mu_0 - \mu_\infty)[1 + (\lambda\gamma)^2]^{(n-1)/2} \tag{3}$$

were used. In Equation 3, γ denotes the rate of strain and the values of the constants were $\lambda = 3.313$ s, $n = 0.3568$, $\mu_\infty = \mu_N = 3.45 \times 10^{-3}$ Pa · s and $\mu_0 = 0.56$ Pa · s.[34] The non–Newtonian viscosity model can be understood as a refinement of the basic Newtonian model as it addresses the fact that blood viscosity should be considerably higher than μ_N in regions featuring comparatively low velocity levels. Note that the higher the value of γ in Eq. (3) (i.e., the higher the blood flow rate) the closer the viscosity, $\mu(\gamma)$, will be to the Newtonian value $\mu_\infty = \mu_N$. From a more theoretical standpoint, since the non–Newtonian model will predict a volume–averaged value of viscosity, $\overline{\mu}(\gamma)$, considerably above μ_N then for a given value of the blood flow rate the mean flow Reynolds number,

$$Re = \frac{\rho |U| d_h}{\overline{\mu}} \tag{4}$$

will be considerably lower than it will be in the corresponding calculation with the Newtonian model. In Equation (4), $|U|$ denotes a characteristic velocity scale, d_h is the IVC hydraulic diameter and $\overline{\mu}$ denotes the volume averaged viscosity. At a given axial location within the IVC the hydraulic diameter is estimated as $d_h = 4A_\perp / P$, where $A_\perp$ and P are the IVC cross-section area and wall perimeter, respectively.

The flow was assumed to be in the laminar regime, an assumption that was confirmed by the current results as the highest Reynolds numbers obtained with the Newtonian and the non–Newtonian viscosity models were respectively $Re = 1,530$ and 860 in the infrarenal region. Notwithstanding, the possibility of unsteady velocity fluctuations in the wake of the filter struts/legs (which pose an obstacle to the blood flow) is also to be considered. A relevant reference in this respect is in the work of Ren et al.[13]. The numerical simulation on a 3D IVC model performed by these authors included the use of a turbulence model. When the IVC model was unoccluded, Ren et al. found no significant levels of turbulent kinetic energy (TKE) even in high exercise conditions ($Re = 1,640$). However, when they partially occluded the IVC model with a spherical clot having a diameter of about $d = 14$ mm, Ren et al. reported that the flow remained laminar at $Re = 360$ but high TKE levels in the wake of the sphere were found at $Re = 1,400$ and $1,640$. In the flow around bluff bodies (e.g., a cylinder or a sphere) the quantity that controls transition to turbulence is the Reynolds number based on the diameter of the body, Re_d. In the present simulations the diameter of the filter struts/legs was at most $d = 0.18$ mm, which yields $Re_d \leq 25$, a value almost two orders of magnitude lower than the one reported by Ren et al. for their simulations under exercise conditions. Thus, for the conditions in the current work the assumption of a laminar flow regime seems to be fully consistent.

2.3 | Post–processing

A quantity of high interest in hemodynamics studies is the wall shear stress (WSS). For each particular flow simulation, surface averaged WSS values were computed on both the IVC wall ($\overline{WSS}_{vein}$) and the filter surface ($\overline{WSS}_{filter}$) by means of numerical integration of the modulus of the local skin friction force along every surface cell (triangle). Special attention was given to the calculation of the total forces exerted by the blood flow on the filter surface. At every computational cell on the filter surface the blood flow exerts two types of forces: viscous skin friction forces, locally tangent to the surface element, and the force exerted by the fluid pressure, normal to the surface. The resultant skin friction force ($\vec{F}_f$) and the resultant pressure force ($\vec{F}_p$) vectors were computed by numerical integration over the whole filter surface. That is, separate surface integrations were respectively performed for the $x-$, $y-$ and $z-$component of each type of force. The corresponding magnitudes (moduli) of these resultant forces are respectively denoted as F_f and F_p. Note therefore that for a filter having a surface area A_{filter} we will always have

$F_f < \overline{WSS}_{filter} A_{filter}$ due to an overall cancellation effect, that is, locally the skin friction force on a surface element is not perfectly well aligned with the main flow direction.

The resultant drag force, i.e., the overall drag exerted by the blood flow on the filter, was then calculated as $\vec{F}_d = \vec{F}_f + \vec{F}_p$ and its modulus is denoted as F_d. Even though F_d is the most relevant quantity in practical terms, the calculated values of both F_f and F_p will also be shown. One may expect that the modulus of the resultant skin friction force will be, for a fixed value of the blood flow rate, roughly proportional to the surface area, that is, $F_f \propto A_{filter}$ in the context of the current study. On the other hand, the total pressure force F_p might be a more qualitative tool that may better reflect the differences in shape of the different filter designs. Those filters having elements, and particularly their struts, aligned more transversally to the main blood flow direction might yield considerably higher F_p values.

In addition, we also assessed the alignment of the different resultant force vectors. Note that due to the realistic geometry of the IVC wall (see Figure 1), the distribution of the blood flow around the filter lacks any kind of symmetry and thus we have $F_d = |\vec{F}_f + \vec{F}_p| < F_f + F_p$. That is, one should expect the $\vec{F}_f$ and $\vec{F}_p$ vectors to be slightly misaligned and, for the same reason, the resultant drag force $\vec{F}_d$ to be slightly misaligned with the main filter axis.

2.4 | Discretization of the conservation equations and testing

The discrete form of Equations (1) and (2) were solved for steady state solutions by means of the SIMPLE algorithm.[34,36] The three–dimensional (3D) volume models used in the CFD simulations consisted of tetrahedral meshes that were generated using the Gmsh software.[37] Several 3D meshes were tested for the IVC base surface model, i.e., with no filter present. Table 2 shows the $\overline{WSS}_{vein}$ values obtained with four different meshes under exercise conditions with both the Newtonian (μ_N) and the non-Newtonian ($\mu(\gamma)$) viscosity model. In meshes A, B and C we used the standard IVC surface model with $n_v = 68,432$ triangles and different values of the numerical parameter, ϕ, that controls the maximum size of 3D elements (tetrahedra). In mesh D a finer surface model ($n_v = 109,152$) was used with the same value for the ϕ parameter as in mesh B. To better assess the effect of mesh refinement on the accuracy of the calculations, the variations of the circumferentially averaged pressure–drop and WSS along the z–axis are shown in Figure 2 for the four meshes. In Figure 2A we see that the two meshes with the largest number of tetrahedra, C and D, produced very similar profiles, with mesh B just slightly underestimating the pressure drop values. In Figure 2B the circumferentially averaged WSS profiles for mesh D are clearly distinguishable from the rest of profiles in the regions around the local maxima and minima. Thus, the accuracy of predicted WSS values depends more strongly on the level of surface refinement than it does on the number of elements (N_t) of the 3D mesh.

Since the discrepancies in both the pressure–drop and WSS predictions obtained with the four meshes (A–D) are modest the surface model with $n_v = 68,432$ triangles, together with the ϕ value used in mesh B, seems to be the best compromise between accuracy and computational cost for subsequently building the 3D meshes in the models having a filter. The 3D meshing software generates tetrahedra whose size increases with the distance to a solid boundary, either the IVC wall or the filter surface. As the smallest size in the surface elements are always found in the filter model it is no surprise that the smallest tetrahedra were located in the vicinity of the filter surface. This effect is illustrated in Figure 3 B–D where velocity and pressure contours and the projection of the 3D mesh are plotted at a given cross-stream section for the calculation under exercise conditions with the

		3D Mesh			
		Mesh A	Mesh B	Mesh C	Mesh D
n_v		68,432	68,432	68,432	109,152
N_t		301,389	396,316	538,731	851,145
$\overline{WSS}_{vein}$ (Pa)	μ_N	1.217	1.230	1.238	1.231
	$\mu(\gamma)$	1.324	1.331	1.336	1.329

TABLE 2 Summary of the test calculations performed in four different 3D meshes for the IVC base case (with no filter) under exercise conditions, a flow rate of $V_{in} = 80$ cm^3/s into the IVC segment and $V_{ren} = 10$ cm^3/s into both the left and right renal vein segments. For each mesh the values of the number of triangles in the IVC surface mesh, n_v, the number of tetrahedra, N_t, and the calculated averaged WSS values on the vein wall, $\overline{WSS}_{vein}$, for both the Newtonian, μ_N, and the non–Newtonian, $\mu(\gamma)$, fluid model are shown.

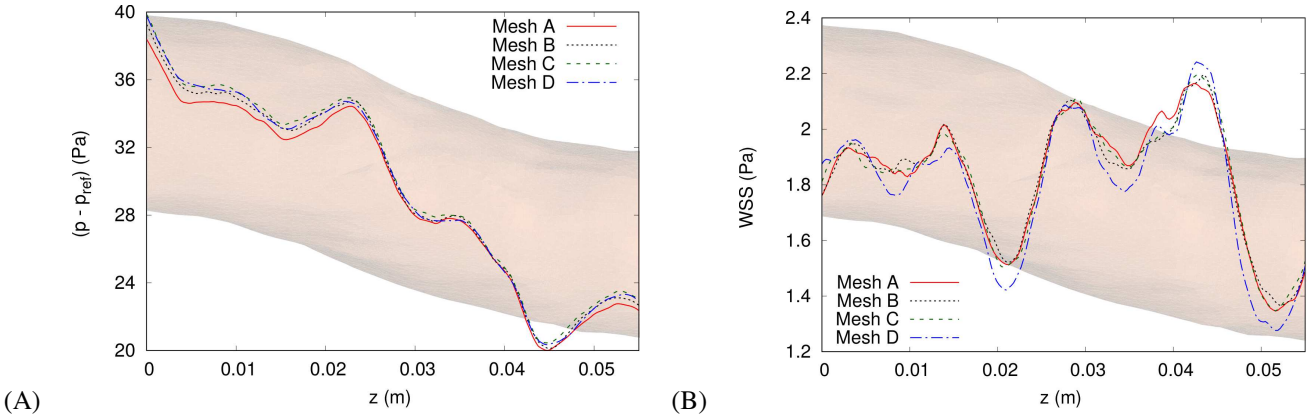

FIGURE 2 Effect of mesh refinement on the variation along the z–axis of the circumferentially averaged (A) pressure–drop and (B) WSS values at a segment of the vein wall in the infrarenal region. Exercise conditions were assumed and the non–Newtonian viscosity model was used. The pressure–drop is defined as $p - p_{ref}$, with p_{ref} being chosen as the average absolute pressure at the IVC outlet section.

filter 2 model and the non–Newtonian viscosity model. The asymmetry in the velocity pattern, caused by the curvature of the IVC wall (see Figure 1), is quite remarkable in Figure 3 B with considerably higher values in the left lower part of the slice. The level of asymmetry was found to increase, in all of the present calculations, with increasing blood flow rate. The broken pattern in the contours in Figure 3 B reflects the passage of the blood flow around the filter struts. These struts, when not aligned with the filter axis, pose an obstacle to the blood flow, as is reflected in the strong pressure fluctuations observed in Figure 3 C. The highest density of (projected) 3D mesh points in Figure 3D is accordingly observed in those zones with a strut or cylinder head nearby. Note that the very high concentration of mesh points around the slice center is due to the fact that the filter 2 model features two different axially–aligned cylinder heads, one of them below and the other one above the slice z–level (Figure 3 A).

	3D Mesh with filter 1		
	Mesh B_1	Mesh D_1	Mesh B_1 embedded
N_t	8,688,857	12,291,357	9,300,624
$\overline{WSS}_{filter}$ (Pa)	10.39	10.35	10.17
F_d (dyne)	115.9	115.2	114.9

TABLE 3 Summary of test calculations performed under exercise conditions for the filter 1 case. The B_1 mesh is based on the standard IVC surface mesh ($n_v = 68,432$). The D_1 mesh is based instead on the finer IVC surface mesh with $n_v = 109,152$. The third mesh is based on the B_1 IVC surface mesh but with the tips of the filter hooks connected to the IVC surface. The N_t entry in the table denotes the number of tetrahedra of the 3D mesh. In all cases the non–Newtonian, $\mu(\gamma)$, fluid model was used.

The size of the 3D meshes in the models having a filter ranged between $N_t = 5,754,523$ and $12,040,516$ tetrahedra, that is, a value much higher than the one needed in the base IVC case (see Table 2). Due to the small size of the triangles in the filter surface meshes the IVC surface mesh had to be locally refined in several patches around the vein wall locations closest to a filter hook or strut. Such a local refinement, tailored to each particular filter model, was applied to the standard IVC surface Mesh B ($n_v = 68,432$). Notwithstanding, an additional 3D mesh was also generated for the filter 1 model on the basis of the finer IVC surface Mesh D ($n_v = 109,152$). The results obtained with the standard and the refined 3D meshes with the filter 1 model

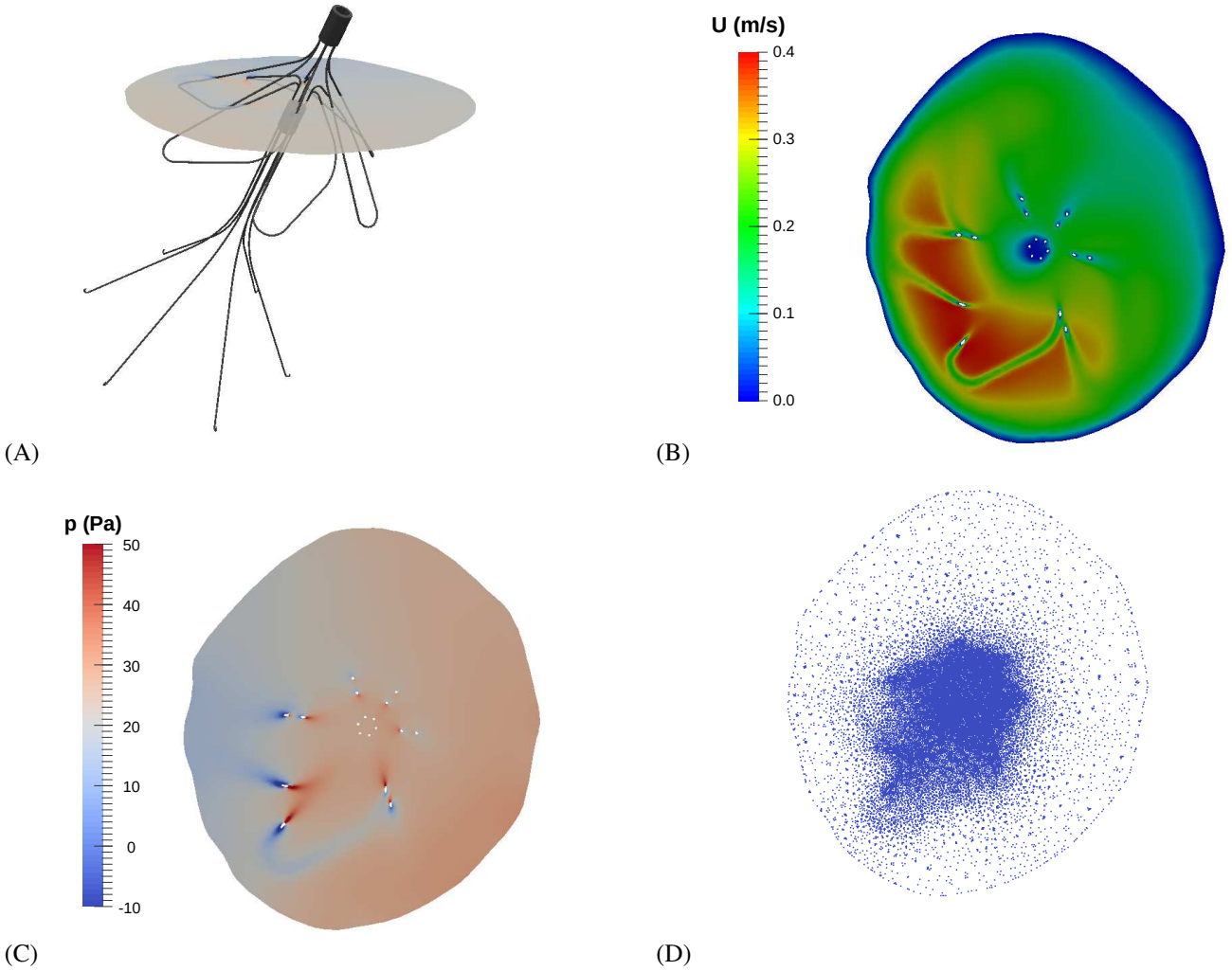

FIGURE 3 Cross–section views for the calculation with the filter 2 model under exercise conditions using the non–Newtonian viscosity model: (B) distribution of velocity (z– component); (C) distribution of pressure–drop; (D) projection of mesh cells. (A) posterior view of the location of the cross–section plane, which has been chosen normal to the z–axis.

are compared in Table 3 for a calculation under exercise conditions with the non–Newtonian viscosity model. The important increase in the number of tetrahedra, from $N_t = 8,668,857$ into $12,291,357$, resulted in just a small variation in the predicted $\overline{WSS}_{filter}$ and F_d values.

A second additional 3D mesh, based on the IVC surface Mesh B, was generated with the filter 1 model to test the effect of the clearance that was assumed between the tips of the filter hooks and the IVC wall; that is, in this additional 3D mesh the hooks were embedded into the vein wall. As can be seen in Table 3, there is a slight increase in the number of tetrahedra in the embedded filter 1 mesh and the predicted F_d and $\overline{WSS}_{filter}$ values are about 1% and 2% lower, respectively. In the standard 3D mesh, the filter hooks are entirely surrounded by blood and the skin friction forces are therefore slightly overpredicted. Notwithstanding, as velocities in the vicinity of the vein wall are quite close to zero, the error introduced by the clearance approach is reasonably small. Moreover, the methodology for embedding the filter hooks into the IVC wall was tedious and error prone. The opening angle of each filter leg had to be slightly modified and patches on the IVC surface mesh close to each particular filter hook had to be individually tuned up.

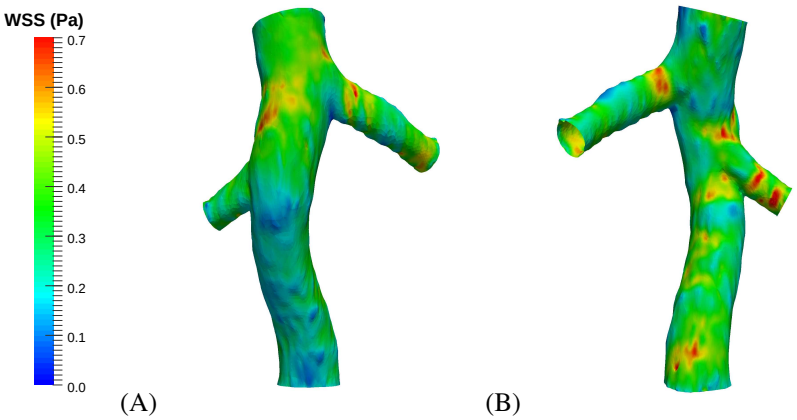

FIGURE 4 (A) Anterior and (B) posterior views of the local WSS distributions on the vein surface for the IVC base case under rest conditions. A non–Newtonian viscosity model was used.

3 | RESULTS

Steady state solutions of Equations (1) and (2) were computed for the IVC base case and each of the cases including a filter model. In each case, four different values of the inlet blood flow rate at the IVC infrarenal section, V_{in}, and at the renal vein sections, V_{ren}, were considered. Most of the results presented here correspond to the rest condition with $V_{in} = 20$ cm^3/s and $V_{ren} = 7$ cm^3/s and the exercise condition with $V_{in} = 80$ cm^3/s and $V_{ren} = 10$ cm^3/s.[18] In addition, two intermediate cases with inlet flood flow rates of $V_{in} = 40$ cm^3/s and $V_{ren} = 8$ cm^3/s and $V_{in} = 60$ cm^3/s and $V_{ren} = 9$ cm^3/s were considered.

The circumferentially averaged WSS profiles in Figure 2B present large peaks and valleys that are a consequence of the curvature (concavity or convexity) of the IVC wall. The effects of the wall curvature are also visible on the local WSS distributions on the IVC wall, such as those shown in Figure 4 for the base case under rest conditions. Note that the WSS levels in the posterior view in Figure 4B are considerably higher than they are in the anterior part of the wall, shown in Figure 4A. Foci with high or low WSS values are closely related to irregularities of the vein geometry, in agreement with previous results by Aycock et al.[17] The corresponding local WSS distributions for other values of blood flow rates, either with the presence or the absence of a filter (not shown here for the sake of brevity) have a similar look as the location and shape of the high/low WSS spots basically coincide. The notion that the presence of a filter does not significantly alter the WSS levels on the IVC wall is confirmed by the surface averaged values, $\overline{WSS}_{vein}$, plotted in Figure 5A,B. The $\overline{WSS}_{vein}$ values for exercise conditions were between 4 and 5 times larger than the corresponding values for rest conditions (Figure 5A,B). The calculated $\overline{WSS}_{filter}$ values are plotted in Figure 5C,D for each of the filter models. Comparing Figure 5A to Figure 5C and Figure 5B to Figure 5D we observe that the $\overline{WSS}_{filter}$ values are roughly one order of magnitude higher than the corresponding $\overline{WSS}_{vein}$ values. Furthermore, there are significant differences in $\overline{WSS}_{filter}$ values among the four filters, being filter 3 the one with the lowest values. Note that an increase of V_{in} by a factor of four (or equivalently, changing from rest to exercise conditions) causes the $\overline{WSS}_{filter}$ values to increase by a factor of about six.

The high $\overline{WSS}_{filter}$ levels in Figure 5C,D suggest that the blood flow is significantly altered by the presence of a filter. As shown in Figure 3B for the case of the filter 2 model, the blood flow is indeed altered when it meets an obstacle such as a filter strut. The corresponding plots for the other filter models, not included here, show a qualitatively similar disruption of the velocity pattern behind the filter elements. In all of the cases, an important velocity deficit was observed in the wake of the filter cylindrical head but most of such deficit was recovered at the end of the infrarenal section. Inspection of Figure 5 also reveals that the viscosity model has a considerable effect on predicted $\overline{WSS}$ values, with the non–Newtonian model yielding higher values in all of the cases investigated. Note that the higher the flow rate the lesser the difference between the predictions of the two viscosity models. For the sake of conciseness, only results of the calculations with the non–Newtonian viscosity model will be shown hereinafter.

The presence of a filter within the IVC will cause the blood flow to exert forces on the filter surface. The magnitudes of the resultant skin friction (F_f) and pressure (F_p) forces as well as the magnitudes of the total drag force (F_d) are plotted in

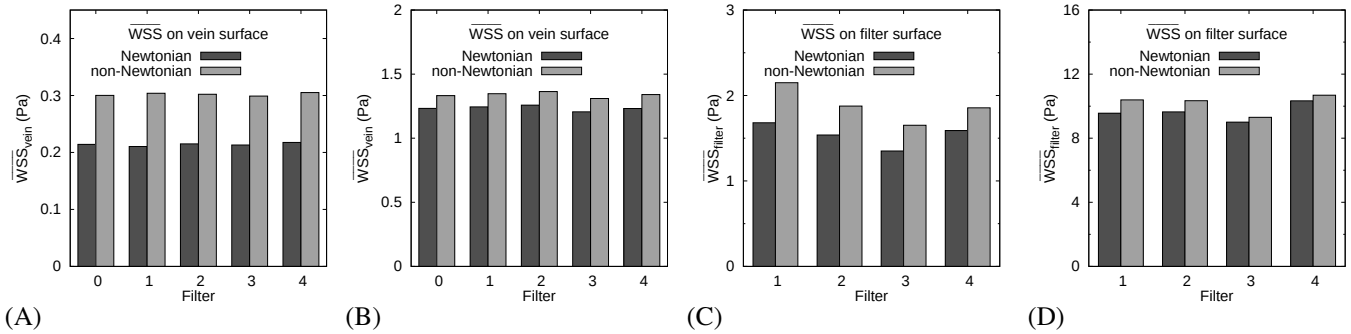

FIGURE 5 Surface–averaged WSS values for the five cases investigated: the IVC base case (label 0) and the filter models (labels 1 to 4). The $\overline{WSS}$ values are shown for (A,C), rest conditions and (B,D), exercise conditions.

Figures 6A–D. The magnitude and direction of the skin friction and pressure forces exerted by the blood flow on each individual component (leg, strut or head) of the filter depend on the angle between the particular component and the main flow direction. In other words, depending on its particular orientation a filter component may act, from a mechanistic point of view, as an obstacle to the blood flow and thus experience comparatively high values of the pressure force. Pressure forces may even be locally stronger than skin friction forces at those parts of the filter components (struts or legs) that are not well aligned with the main blood flow. For example, we can infer in Figure 3C a pressure drop of about 60 Pa around the filter struts when the maximum local WSS values observed on the filter struts were about 40 Pa in the same calculation with the filter 2 model.

Figures 6A,C show the calculated values of F_f and F_p on each of the filter surfaces under rest and exercise conditions, respectively. Note that filter 3, the one with the largest surface area, yields F_p values between 2.5 and 3.5 times smaller than

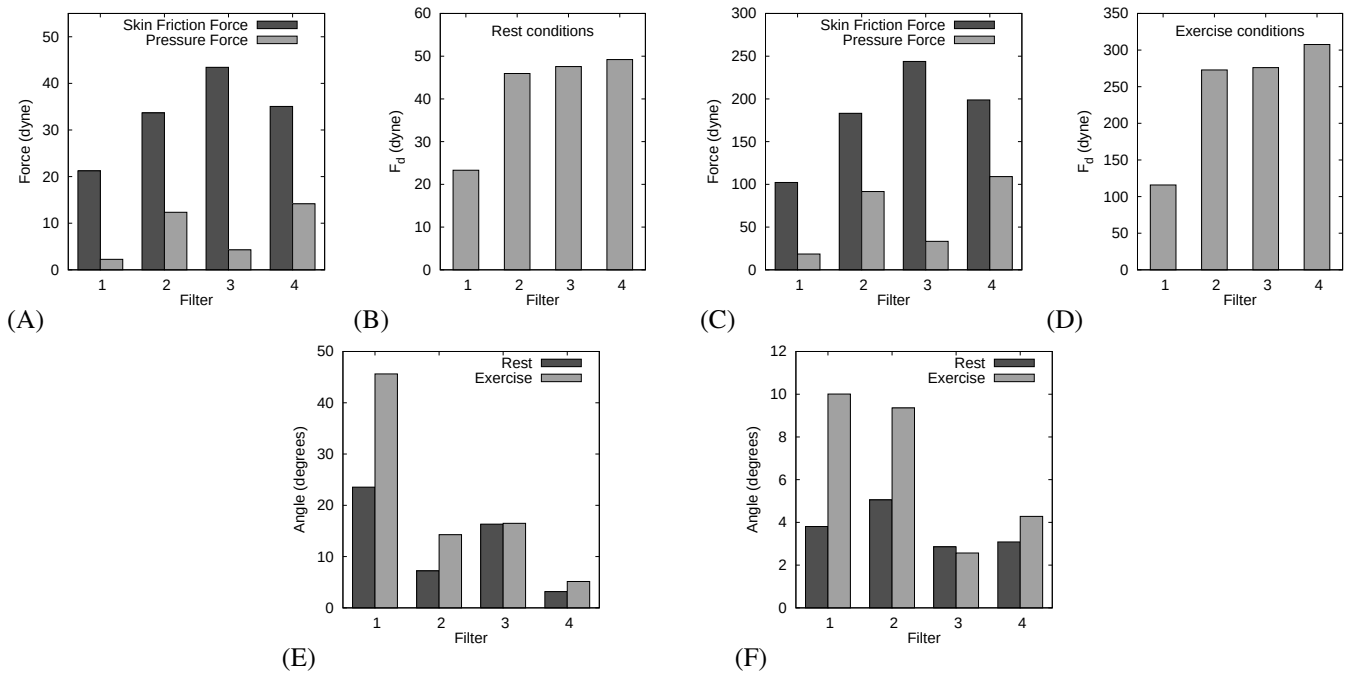

FIGURE 6 (A,C), Magnitudes of the resultant skin friction force (F_f) and pressure force (F_p) exerted on the filter surface for the four filter models investigated, calculated under (A) rest and (C) exercise conditions. (B,D), Magnitude of the total drag force (F_d) exerted on the filter surface under (B) rest and (D) exercise conditions. (E) Angle between $\vec{F}_f$ and $\vec{F}_p$. (F) Angle between $\vec{F}_d$ and the filter axis.

the values obtained for filters 2 and 4, thus confirming the notion that F_p is much less dependent on A_{filter} than F_f is. It is not surprising that the simple design of filter 1 (see Figure 1) produces the smallest F_p values. Note that when the skin friction and pressure forces are added filter 4 is the one yielding the highest F_d values and filter 3, despite its considerably larger surface area, yields F_d values just a little higher than filter 2 (see Figures 6B,D). Filter 1 is the one yielding F_d values much smaller than the rest of the filters, specially under exercise conditions.

Despite the axial symmetry of the filter models, the asymmetry of the blood flow induces a certain degree of misalignment between both $\vec{F}_f$ and $\vec{F}_p$ and the filter axis. As expected, we found that the F_f values for each filter model were roughly proportional to the respective surface area of the filters (see Table 1). We also found that $\vec{F}_f$ was in all of the cases investigated well aligned with the filter axis, with maximum departures below 5 degrees. The degrees of misalignment between $\vec{F}_f$ and $\vec{F}_p$ and between $\vec{F}_d$ and the filter axis are respectively shown in Figures 6E,F. Filters 1 and 2 yield the highest $\vec{F}_d$ misalignment in Figure 6F, specially under exercise conditions where the angle for both filters is between 9 and 10 degrees. These maximum angles remain rather small because filter 1, presenting a high misalignment between $\vec{F}_f$ and $\vec{F}_p$ (see Figure 6E), yields the lowest F_p values whereas filter 2, yielding comparatively high F_p values, shows a modest misalignment between $\vec{F}_f$ and $\vec{F}_p$. An IVC filter is said to tilt when its misalignment exceeds 10[25] or 15[38] degrees and our results therefore suggest that none of the filter models investigated presents a clear tendency to tilt.

The F_d values are especially relevant as the total force exerted by the blood flow on the filter is counterbalanced by the total force exerted by the filter hooks/struts on the vein wall. Notwithstanding, F_d is an extensive quantity, i.e., it is strongly dependent on dimensional parameters such as the filter surface area and the blood flow rate. In studies of flows around bluff bodies the dimensionless quantities known as friction (C_f) and drag (C_d) coefficients are commonly used. In the context of the current work, these coefficients are defined as,

$$C_f = \frac{2F_f}{\rho \overline{U}_\perp^2 A_{filter}} \tag{5}$$

$$C_d = \frac{2F_d}{\rho \overline{U}_\perp^2 A_{filter}} \tag{6}$$

where A_{filter} is the surface area of the filter and $\overline{U}_\perp$ is the mean blood velocity in a cross–section which is chosen to be normal to the filter axis and slightly upstream of the axial location where the filter begins (so that the blood flow in this section is not yet perturbed by the presence of the filter). Friction and drag coefficients are valuable because they allow a qualitative comparison on the effect of the presence of the bluff body on the flow that surrounds it. That is, in terms of C_f and C_d it is the shape of the object that makes the difference, not its particular size.

Moreover, given an object of a particular shape, the C_f and C_d coefficients are commonly found to depend only on the Reynolds number, Re. Figure 7 shows the dependency on the Reynolds number (based on $\overline{U}_\perp$, see Equation (4)) of the calculated C_f and C_d values for the four filter models. In the friction coefficient plot of Figure 7A filter 1 produces the highest C_f at the lowest blood flow rate and filter 3 is the one yielding the lowest C_f at any V_{in} value. The general trend as V_{in} increases is that the differences in the predicted C_f values between filters 1, 2 and 4 decrease. Figure 7B shows important differences among the predicted values of the drag coefficient, C_d, for the different filter models, being filter 3 the one yielding the lowest C_d values for any blood flow rate. In particular, at the lowest blood flow rate of $V_{in} = 20\text{cm}^3/\text{s}$, corresponding to rest conditions, the predicted C_d values for filter 4 in Figure 7B are almost 40% higher than they are for filter 3.

In all of the cases investigated the calculated C_f and C_d values fitted very well to trend lines in the form $C_f = a_f Re^{b_f}$ and $C_d = a_d Re^{b_d}$, respectively. The values of the parameters of the fits, a_f, b_f, a_d and b_d, are included in Table 4. Note that all of the b_f and b_d exponents in Table 4 are negative but clearly larger than -1. We can combine Equations (4) and (6) with the C_d fit ($C_d = a_d Re^{b_d}$) to obtain

$$F_d = \left(\frac{1}{2} a_d A_{filter} d_h^{b_d} \rho^{b_d+1}\right) \overline{U}_\perp^{2+b_d} \mu^{-b_d} = K \overline{U}_\perp^{2+b_d} \mu^{-b_d} \tag{7}$$

That is, if for a given filter the total drag force was to be proportional to the blood flow rate, $F_d \propto V_{in}$, then on account of Equation (7) we would have $b_d \approx -1$. Thus, $b_d > -1$ means that the predicted dependence of F_d on V_{in} is superlinear. Such a superlinear dependency can also be seen by comparing the F_d values in Figures 6B ($V_{in} = 20\,\text{cm}^3/\text{s}$) and 6D ($V_{in} = 80\,\text{cm}^3/\text{s}$): for each specific filter a fourfold increase of blood flow rate yields an almost sixfold increase of the total drag force exerted on the filter.

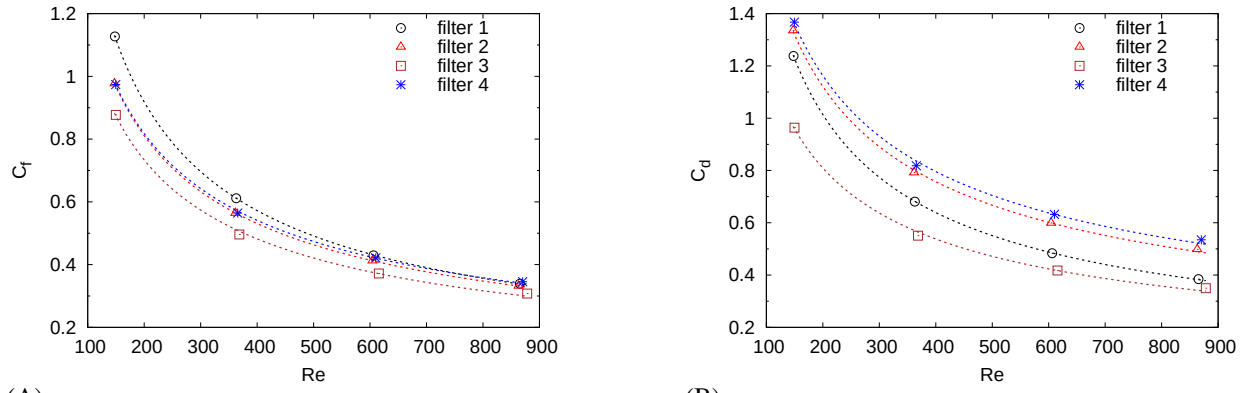

(A) (B)

FIGURE 7 (A) Friction coefficients (C_f) and (B) drag coefficients (C_d) as a function of the Reynolds number for the four filters investigated. Symbols correspond to the calculations with each of the four blood flow cases investigated whereas lines represent the best fitting curves of the form $C_f = a_f Re^{b_f}$ and $C_d = a_d Re^{b_d}$; see Table 4 for the values of the best fit parameters.

4 | DISCUSSION AND CONCLUSIONS

In the present study we used CFD simulations to investigate the effects of IVC filters on hemodynamics. Given a realistic IVC morphology, reconstructed from CT images of a patient, we inserted four different filter models in the blood flow (see Figure 1). Filter 1 has the most classical, simple conical shape and features the least surface area, roughly by a factor of two compared to the rest of the filter models (see Table 1). As a consequence, the filter 1 model yields the smallest total skin friction, F_f, and total pressure, F_p, forces (see Figures 6 A,C). Filters 2 and 4 are the ones yielding F_p values that are, for exercise conditions, at least half of the corresponding F_f values. The high F_p values are a consequence of a more complex filter design with filter components (struts, legs) somewhat transversal to the main blood flow (see Figures 3B,C). In filter 2, a basket–like structure is superimposed to the basic conical shape whereas filter 4 features instead a distinct, double basket structure (see Figure 1). The refinement introduced in these designs, devised to enhance the filter ability to capture small blood clots and to strengthen the attachment to the vein wall, comes at a price in terms of increased values of both F_f (a direct consequence of the increased surface area) and F_p. The notion that the presence of high F_d values may contribute to longterm mechanical fatigue is qualitatively consistent with the relatively high rate of strut fractures reported for the real counterpart of filters 2 and 4[29,39] and the very high (92%) occurrence rate of IVC perforation (without clinical sequelae) reported for the real filter 2.[29]

Filter 3 features a novel design in which an eight leg conical shape is attached to lateral stabilizers with anchors. This filter can be converted into a stent by removing the hub at the filter tip, which allows the filter legs to fold againt the IVC wall.[25] It is

	Filter			
	1	2	3	4
a_f	34.2 ± 0.3	20.7 ± 0.1	18.2 ± 1.4	19.2 ± 0.8
b_f	-0.683 ± 0.001	-0.611 ± 0.001	-0.606 ± 0.014	-0.596 ± 0.008
a_d	34.4 ± 0.4	22.5 ± 1.1	18.4 ± 1.7	21.0 ± 1.7
b_d	-0.665 ± 0.002	-0.566 ± 0.009	-0.589 ± 0.017	-0.547 ± 0.014

TABLE 4 Parameters of the best fitting curves as a function of the Reynolds number for skin friction coefficients, $C_f = a_f Re^{b_f}$, and total drag coefficients, $C_d = a_d Re^{b_d}$, for each of the four filters.

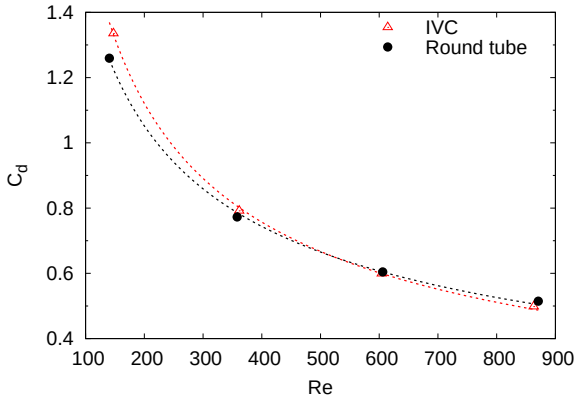

FIGURE 8 Drag coefficients as a function of the Reynolds number for the calculations with the filter 2 model placed in a 20 cm long straight round tube with a 20 mm inner diameter. The corresponding C_d results obtained with filter 2 in the realistic IVC geometry, already plotted in Figure 7, are also included. Dashed lines denote the best fit in the form $C_d = a_d Re^{b_d}$. The values of the fit parameters for the round tube calculations are $a_d = 14.9 \pm 0.9$, $b_d = -0.500 \pm 0.011$.

remarkable that filter 3, with an area some 30% larger than filters 2 and 4, yields similar F_d values (see Figure 6B,D). Filter 3 features in fact the most efficient design from an intensive point of view as it yields the lowest C_d values for all of the blood flow rates investigated (see Figure 7B). Moreover, filter 3 yields F_p values considerably lower than filters 2 and 4 (Figure 6A,C). Such an advantage for filter 3 is due to the fact that its lateral stabilizers are located near the IVC wall, i.e., a region where the blood velocity levels are comparatively low. The real counterpart of filter 3 has been recently the subject of a clinical study[40] in which a very high success rate, with no major complications within six months after filter conversion, was reported. Notwithstanding, as pointed out by Hohenwalter et al.[40] themselves, further studies are necessary to determine long–term safety and efficacy of the (real) filter 3 design.

In the present calculations we used both the Newtonian and a non–Newtonian viscosity model. We found, in agreement with Aycock et al.,[17] that for any given combination of filter model and blood flow rate the non–Newtonian viscosity model always yielded higher $\overline{WSS}$ and F_d values than it did the Newtonian model. Aycock et al. reported that, on the average, the Newtonian model underestimated $\overline{WSS}$ values by about 29%. The corresponding percentages in our calculations were, on the average, about 29% and a 8% in $\overline{WSS}$ underestimation under rest and exercise conditions, respectively.

Anticoagulant drugs are sometimes prescribed to patients having IVC filters implanted. From a hemodynamic point of view, the presence of anticoagulants may decrease the blood viscosity by up to 40%. In turn, a decrease in blood viscosity implies an increase in the Reynolds number (see Equation 4). As can be inferred from Figure 7B, for a given blood flow rate the value of the drag coefficient C_d will be decreased as we move to the right along the abscissae axis. Thus, the administration of anticoagulant drugs would result in a decrease of the total drag force exerted by the blood flow on the filter (see Equation 7). For instance, let us assume a fixed blood flow rate and a 20% reduction of blood viscosity caused by drugs, then Equation 7 gives a decrease in F_d in the 12–15% range depending on the particular filter model (see Table 4). Thus, we present a novel method to estimate the reduction on the force exerted by the IVC filter on the vein wall when an anticoagulant treatment is prescribed.

The drag forces, drag coefficients and their fits were computed in an additional case with a simplified geometry, namely the filter 2 model was placed within a straight round tube with a diameter of 20 mm. As we can see in Figure 8 there is a good resemblance between the predicted drag coefficients obtained with the simplified tube geometry and those obtained with the IVC model (already shown in Figure 7B). We conclude that differences in drag forces and coefficients are far more dependent on the shape and surface area of the filters than they are on the geometry of the vein.

Some previous studies[12,13,16,17] investigated the effects on the blood flow of a partial occlusion of the IVC caused by a blood clot trapped by the filter. The clot sizes in these studies are typically in the range 250–2000 mm^3. For the smallest clot size investigated (250 mm^3) Singer et al[12] reported that the presence of the clot increased the peak WSS values on the IVC wall by about a 40%. Aycock et al[17] found that for a bigger clot of 1060 mm^3 the average WSS on the IVC wall increased from 2.22 to 2.53 Pa. Thus, it seems that clots smaller than 250 mm^3 would not significantly alter the blood flow and would produce just a modest increase on the WSS levels on the vein wall. We however wondered what would be the effect of small blood clots on the

the total drag force, F_d, exerted on the filter. To this purpose we performed additional calculations with the filter 2 model having incorporated, as shown in Figure 9, a lower conic–shaped clot of 114.6 mm^3 plus an upper toroidal–shaped clot of 14.9 mm^3. The size and shape of the clot models is based on studies that include data on clot size and morphology in actual patients[30,41] and silicon made clot models.[11,42]

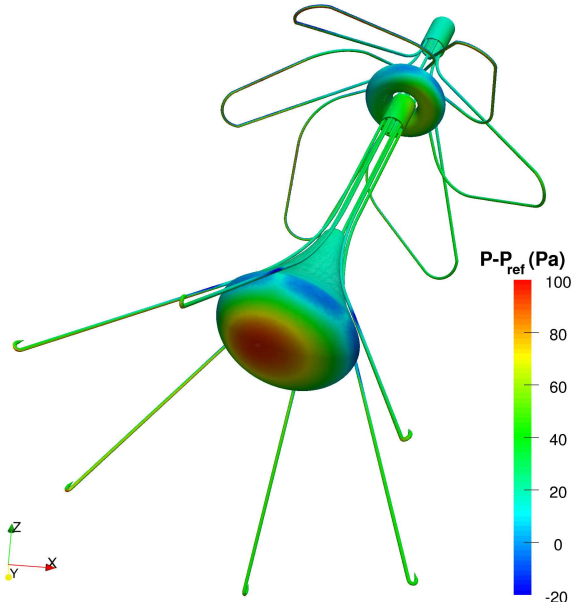

FIGURE 9 Distribution of the pressure–drop on the surfaces of the filter 2 and two blood clot models. The calculation was performed under exercise conditions.

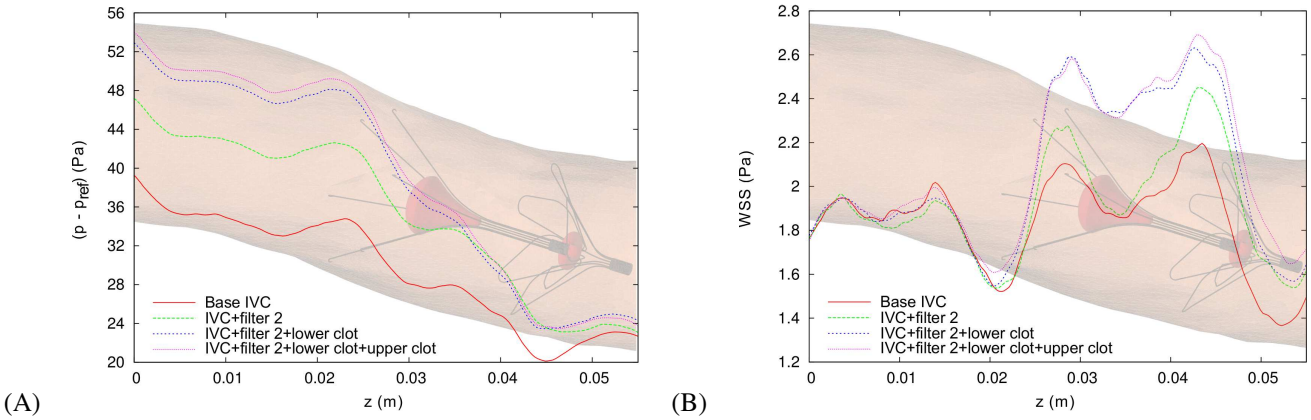

FIGURE 10 Variation along the z–axis of the circumferentially averaged values of (A) pressure–drop and (B) WSS on the vein wall surface. Three cases are compared: filter 2 without a clot, filter 2 with a lower (cone–shaped) clot and filter 2 with both a lower and upper (torus–shaped) clot. All of these calculations were performed under exercise conditions. The base IVC case with no filter is also included.

As shown in Figure 9, the calculations under exercise conditions revealed variations of relative pressure on the clot surface between -20 and 100 Pa. Figure 10A,B respectively show the circumferentially averaged pressure–drop and WSS profiles on

the vein wall. The increase of the pressure–drop with respect to the base non–filter case is around 20% when only the filter is included, around 32% for the filter with only the lower clot and around 34% for the filter with both clots included. Similar levels of increase are observed for the peak values in the WSS profiles of Figure 10B. Moreover, the presence of the two blood clots produces a small increase of the averaged WSS on the whole IVC surface from 1.364 Pa (Figure 5B) to 1.414 Pa. Although we found, in agreement with previous studies,[12,17] that the presence of small clots induces just a small increase in WSS levels a different matter is how it affects the total drag force exerted by the blood flow. For the filter 2 alone this magnitude was $F_d = 45.95$ dyne in the non–exercise case and $F_d = 272.90$ dyne in the exercise case (see Figures 6 B,D). The corresponding values when both clots are included are $F_d = 63.70$ and $F_d = 439.07$ dyne respectively, that is, the total drag force respectively increases by 39% and by 61% in the non–exercise case and the exercise case. Thus, if clots as small as the ones considered here produce increases of more than 50% in F_d, large clots might produce more dramatic effects in regard of total drag and potentially harm the attachment locations at the vein wall.

In summary, even though IVC filters are commonly prescribed when anticoagulant therapy is contraindicated its safety and effectiveness are still in dispute. The reasons for such an uncertainty are to be found in the large variety of filter brands available in the market, the diverse casuistic of patients to whom the filters are inserted and the low percentage of long–term patient follow–up. Except for some notable exceptions (e.g., the PREPIC study[8]), the scarcity of large-scale, prospective clinical studies limits the understanding of adverse issues associated with the use of IVC filters. In this respect, it is worth mentioning the PREPIC2[9] and PRESERVE[43] studies that have been recently endeavored to address this problem. The present results suggest that CFD simulations would be a valuable tool to complement clinical studies. That is, we have investigated how four different IVC filter designs may differently affect the same patient, an objective not achievable by means of in vivo experiments, and to what extent a particular filter design determines the value of the forces that try to drag the filter through the blood stream.

CONFLICT OF INTEREST STATEMENT

None of the authors have financial or personal conflict of interest with regard to this study.

ACKNOWLEDGEMENT

Financial support for the current research was granted by Universitat Rovira i Virgili, projects number 2015PFR-URV-B2-66 and 2016PFR-URV-B2-66.

References

1. Mozaffarian Dariush, Benjamin Emelia J., Go Alan S., Arnett Donna K., Blaha Michael J.. Heart Disease and Stroke Statistics–2016 Update. A Report From the American Heart Association. *Circulation.* 2016;133:e38–e360.

2. Lenchus Joshua D., Biehl Michelle, Cabrera Jorge, Gallo de Moraes Alice, Dezfulian Cameron. In-hospital Management and Follow-Up Treatment of Venous Thromboembolism: Focus on New and Emerging Treatments. *J Intensive Care Med.* 2016;.

3. Kearon Clive, Akl Elie A., Ornelas Joseph, et al. Antithrombotic Therapy for VTE Disease. CHEST Guideline and Expert Panel Report. *CHEST.* 2016;149(2):315–352.

4. Yunus Tahir E., Tariq Nabil, Callahan Rose E., et al. Changes in inferior vena cava filter placement over the past decade at a large community-based academic health center. *J Vasc Surg.* 2008;47(1):157–165.

5. Kim Hyun S., Young Mark J., Narayan Anand K., Hong Kelvin, Liddell Robert P., Streiff Michael B.. A comparison of clinical outcomes with retrievable and permanent inferior vena cava filters. *J Vasc Interv Radiol.* 2008;19:393–399.

6. Decousus Hervé, Leizorovicz Alain, Parent Florence, et al. A clinical trial of vena cava filters in the prevention of pulmonary embolism in patients with proximal deep–vein thrombosis. *New Engl J Med.* 1998;338(7):409–415.

7. Streiff Michael B.. Vena caval filters: a comprehensive review. *Blood.* 2000;95(12):3669–3677.

8. The PREPIC Study Group . Eight-Year Follow-Up of Patients With Permanent Vena Cava Filters in the Prevention of Pulmonary Embolism. The PREPIC (Prévention du Risque d'Embolie Pulmonaire par Interruption Cave) Randomized Study. *Circulation.* 2005;112:416–422.

9. Mismetti Patrick, Laporte Silvy, Pellerin Olivier, et al. Effect of a Retrievable Inferior Vena Cava Filter Plus Anticoagulation vs Anticoagulation Alone on Risk of Recurrent Pulmonary Embolism. A Randomized Clinical Trial. *JAMA.* 2015;313(16):1627–1635.

10. Zhang Fuxian, Li Dajun, Liu Jianlong, Zhang Huan. The Vena Tech LP Permanent Caval Filter: Effectiveness and Safety in the Clinical Setting in Three Chinese Medical Centers. *Thromb Res.* 2015;136:40–44.

11. Stewart Sandy F. C., Robinson Ronald A., Nelson Robert A., Malinauskas Richard A.. Effects of Thrombosed Vena Cava Filters on Blood Flow: Flow Visualization and Numerical Modeling. *Ann Biomed Eng.* 2008;36(11):1764–1781.

12. Singer Michael A., Henshaw W. D., Wang Stephen L.. Computational Modeling of Blood Flow in the TrapEase Inferior Vena Cava Filter. *J. Vasc. Interv. Radiol.*. 2009;20(6):799–805.

13. Ren Zhuyin, Wang Stephen L., Singer Michael A.. Modeling hemodynamics in an unoccluded and partially occluded inferior vena cava under rest and exercise conditions. *Med. Biol. Eng. Comput.*. 2012;50:277–287.

14. Nicolás M., Malvé M., Peña E., Martínez M. A., Leask R.. In vitro comparison of Günther Tulip and Celect filters. Testing filtering efficiency and pressure drop. *J Biomech.* 2015;48:504–511.

15. Nicolás M., Palero V. R., Peña E., Arroyo M. P., Martínez M. A., Malvè M.. Numerical and experimental study of the fluid flow through a medical device. *Int Commun Heat Mass.* 2015;61:170–178.

16. Aycock Kenneth I., Campbell Robert L., Manning Keefe B., et al. A Computational Method for Predicting Inferior Vena Cava Filter Performance on a Patient–Specific Basis. *J Biomech Eng-T ASME.* 2014;136(8).

17. Aycock Kenneth I., Campbell Robert L., Lynch Frank C., Manning Keefe B., Craven Brent A.. The Importance of Hemorheology and Patient Anatomy on the Hemodynamics in the Inferior Vena Cava. *Ann Biomed Eng.* 2016;44(12):3568–3582.

18. Cheng Christopher P., Herfkens Robert J., Taylor Charles A.. Inferior vena caval hemodynamics quantified in vivo at rest and during cycling exercise using magnetic resonance imaging. *Am J Physiol Heart Circ Physiol.* 2003;284:H1161–H1167.

19. 3DSlicer . *A multi-platform, free and open source software package for visualization and medical image computing.* https://www.slicer.org/. Accessed 10-Nov-2017; 2017.

20. Blender Foundation . *Blender. Open Source 3D creation.* https://www.blender.org/. Accessed 10-Nov-2017; 2017.

21. Boston Scientific . *Greenfield™ vena cava filters.* http://www.bostonscientific.com/en-US/products/embolic-protection/greenfield-vena-cava-filter.html. Accessed 10-Nov-2017; 2017.

22. Bard PV . SIMON NITINOL® *Vena Cava Filter.* http://www.bardpv.com/portfolio/simonnitrol/. Accessed 10-Nov-2017; 2017.

23. B. Braun Interventional Systems . *VenaTech® Convertible ™ Vena Cava Filter System.* http://www.bisusa.org/products/vena-cava-filters/venatech-convertible-vena-cava-filter-system. Accessed 10-Nov-2017; 2017.

24. Cordis . *OPTEASE® Retrievable Vena Cava Filter.* https://www.cordis.com/en_us/endovascular/intervene/vena-cava-filters/optease-retrievable-vena-cava-filter.html. Accessed 10-Nov-2017; 2017.

25. Rajasekhar Anita, Streiff Michael B.. Vena cava filters for management of venous thromboembolism: A clinical review. *Blood Reviews.* 2013;7:225–241.

26. Proctor Mary C., Cho Kyung J., Greenfield Lazar J.. In Vivo Evaluation of Vena Caval Filters: Can Function Be Linked to Design Characteristics?. *Cardiovasc Intervent Radiol.* 2000;23:460–465.

27. Kiguchi Misaki M., Dillavou Ellen D.. Inferior Vena Cava Filters. In: Gahtan Vivian, Costanza Michael J., eds. *Essentials of Vascular Surgery for the General Surgeon*, New York: Springer-Verlag 2015 (pp. 183–198).

28. Alkhouli Mohamad, Morad Mohammad, Narins Craig R., Raza Farhan, Bashir Riyaz. Inferior Vena Cava Thrombosis. *JACC: Cardiovascular Interventions.* 2016;9(7):630–643.

29. Poletti P. A., Becker C. D., Prina L., et al. Long–term results of the Simon nitinol inferior vena cava filter. *Eur. Radiol.*. 1998;8:289–294.

30. Nutting Charles, Coldwell Douglas. Use of a TrapEase Device as a Temporary Caval Filter. *J Vasc Interv Radiol.* 2001;12:991–993.

31. code aster . *Salome–Meca. code aster. Structures and Thermomechanics Analysis for Studies and Research.* http://www.code-aster.org/spip.php?article303. Accessed 10-Nov-2017; 2017.

32. Van Ha Thuong G.. Complications of Inferior Vena Caval Filters. *Semin Intervent Radiol.* 2006;23:150–155.

33. The OpenFOAM Foundation . *OpenFOAM.* http://openfoam.org/. Accessed 10-Nov-2017; 2017.

34. Fortuny G., Herrero J., Puigjaner D., et al. Effect of anticoagulant treatment in deep vein thrombosis: a patient–specific computational fluid dynamics study. *J Biomech.* 2015;48:2047–2053.

35. Bird R. Byron, Amstrong Robert C., Hassager Ole. *Dynamics of Polimeric Liquids*. New York: John Wiley & Sons; second ed.1987.

36. Ferziger Joel H., Perić Milovan. *Computational Methods for Fluid Dynamics*. Berlin: Springer–Verlag; third ed.2002.

37. Geuzaine Christophe, Remacle Jean-François. *Gmsh. A three–dimensional finite element mesh generator with built–in pre– and post–processing facilities.* http://gmsh.info/. Accessed 10-Nov-2017; 2017.

38. Grewal Simer, Chamarthy Murthy R., Kalva Sanjeeva P.. Complications of inferior vena cava filters. *Cardiovasc Diagn Ther.* 2016;6:632–641.

39. Wang Stephen L., Siddiqui Arsalan, Rosenthal Elan. Long–term complications of inferior vena cava filters. *J Vasc Surg–Venous L.* 2017;5(1):33–41.

40. Hohenwalter Eric J., Stone James R., O'Moore Paul V., et al. Multicenter Trial of the VenaTech Convertible Vena Cava Filter. *J Vasc Interv Radiol.* 2017;28:1353–1362.

41. Teo Terence K. B., Angle John F., Shipp John I., et al. Incidence and Management of Inferior Vena Cava Filter Thrombus Detected at Time of Filter Retrieval. *J Vasc Interv Radiol.* 2011;22:1514–1520.

42. Wang Stephen L., Timmermans Hans A., Kaufman John A.. Estimation of Trapped Thrombus Volumes in Retrievable Inferior Vena Cava Filters: A Visual Scale. *J Vasc Interv Radiol.* 2007;18:273–276.

43. The IVC Filter Study Group Foundation . *Predicting the Safety and Effectiveness of Inferior Vena Cava Filters (PRESERVE).* http://www.preservetrial.com. Accessed 10-Nov-2017; 2017.

How to cite this article: López J M, Fortuny G, Puigjaner D, Herrero J and Marimon F ( ), A comparative CFD study of four inferior vena cava filters, *Int J Numer Meth Biomed Engng.*, .